CrossMark

ORIGINAL PAPER

S. J. D. D'Alessio

Flow past a slippery cylinder: part 2 - elliptic cylinder

Abstract Part 2 of this paper is devoted to two-dimensional unsteady flow of a viscous incompressible fluid past an inclined elliptic cylinder subject to impermeability and Navier slip conditions on the surface. As in Part 1, the flow is calculated using two methods: an approximate analytical solution in the form of an asymptotic expansion and a numerical solution based on a spectral-finite difference scheme. The results reveal excellent agreement between the analytical and numerical solutions for small times and moderately large Reynolds numbers. Extensive results focussing on asymmetrical flows are presented for Reynolds numbers 500 and 1000 for various aspect ratios, inclinations, and slip lengths. Comparisons with the no-slip case are also made to elicit the effects of the Navier slip condition. The main findings include a reduction in drag as well as a suppression in vortex shedding.

1 Introduction and mathematical formulation

Outlined in Part 1 were various underlying assumptions. These include the impulsive start at $t = 0$ whereby the cylinder moves with uniform speed U_0 in the positive x direction through a viscous incompressible fluid. The flow is then assumed to remain laminar and two dimensional for all time, t. We continue with these assumptions in Part 2 and discuss the more general flow past an inclined elliptic cylinder. As a result of the more complicated geometry, there are several subtleties that arise, and these will be explained in detail. We begin by formulating the governing equations and corresponding boundary and initial conditions in a coordinate system that is best suited for the problem. Following that, the problem is then cast into boundary-layer coordinates to better resolve the early development of the flow. An analytical solution that describes the early stages of the flow is then constructed. A numerical method for solving the governing equations is also presented. Following that, results and comparisons are discussed, and lastly, the key findings are summarized in the conclusions. An Appendix outlining the derivation of the drag, lift, and pressure coefficients is also included.

The problem we are interested in is illustrated in Fig. 1, which shows an elliptic cylinder inclined at an angle of α with respect to the horizontal. The x- and y-axes are oriented along the major and minor axes of the ellipse, where a, b denote the semimajor and semiminor axes lengths, respectively. We define the aspect ratio, r, as the ratio of the minor to major axis of the ellipse (i.e., $r = b/a$) with $0 < r < 1$. We note that $r = 0$ corresponds to a flat plate while $r = 1$ a circular cylinder. Posed in Cartesian coordinates and in dimensionless form, the Navier–Stokes equations are given by

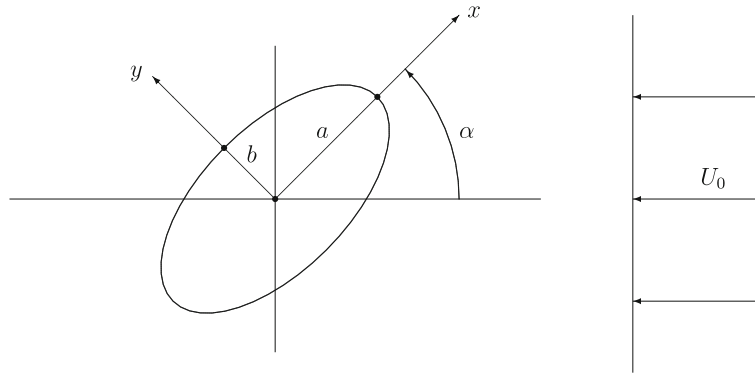$$\frac{\partial^2 \psi}{\partial x^2} + \frac{\partial^2 \psi}{\partial y^2} = \zeta, \tag{1}$$

S. J. D. D'Alessio (✉)
Department of Applied Mathematics, University of Waterloo, Waterloo, ON N2L 3G1, Canada
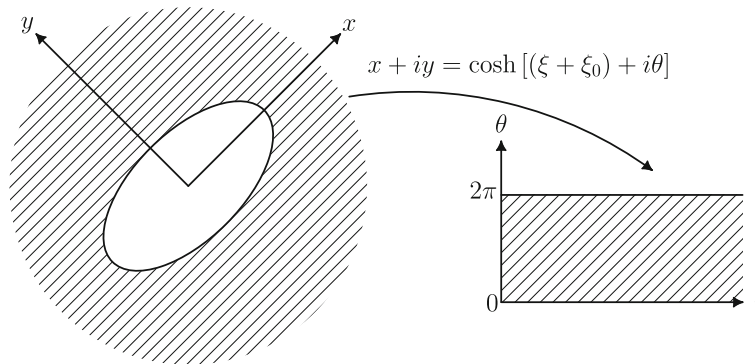E-mail: sdalessio@uwaterloo.ca

Fig. 1 The flow setup

Fig. 2 Conformal transformation

$$\frac{\partial \zeta}{\partial t} = \frac{\partial \psi}{\partial y}\frac{\partial \zeta}{\partial x} - \frac{\partial \psi}{\partial x}\frac{\partial \zeta}{\partial y} + \frac{2}{R}\left(\frac{\partial^2 \zeta}{\partial x^2} + \frac{\partial^2 \zeta}{\partial y^2}\right). \tag{2}$$

Here, the dimensionless stream function, ψ, and vorticity, ζ, are related to their dimensional counterparts, ψ^*, ζ^* through $\psi^* = cU_0\psi$ and $\zeta^* = U_0\zeta/c$, where $c = \sqrt{a^2 - b^2}$ is the semi-focal length of the ellipse. The dimensionless time t is related to the dimensional time t^* by $t^* = ct/U_0$, and the dimensionless coordinates are related by $(x^*, y^*) = c(x, y)$. Lastly, R denotes the Reynolds number defined by $R = 2cU_0/\nu$, where ν is the kinematic viscosity.

A more convenient coordinate system is introduced by the conformal transformation

$$x + iy = \cosh[(\xi + \xi_0) + i\theta], \tag{3}$$

which, as shown in Fig. 2, transforms the contour of the ellipse into $\xi = 0$, $\theta = 0$ to the positive x-axis, and the infinite region exterior to the cylinder to the semi-infinite rectangular strip $\xi \geq 0$, $0 \leq \theta \leq 2\pi$. The constant ξ_0 appearing in (3) is defined by $\tanh \xi_0 = r$. In terms of the modified polar coordinates (ξ, θ), the governing equations become

$$\frac{\partial^2 \psi}{\partial \xi^2} + \frac{\partial^2 \psi}{\partial \theta^2} = M^2\zeta, \tag{4}$$

$$M^2\frac{\partial \zeta}{\partial t} = \frac{\partial \psi}{\partial \theta}\frac{\partial \zeta}{\partial \xi} - \frac{\partial \psi}{\partial \xi}\frac{\partial \zeta}{\partial \theta} + \frac{2}{R}\left(\frac{\partial^2 \zeta}{\partial \xi^2} + \frac{\partial^2 \zeta}{\partial \theta^2}\right). \tag{5}$$

In the above, M refers to the metric of the transformation and is given by

$$M^2 = \frac{1}{2}[\cosh[2(\xi + \xi_0)] - \cos(2\theta)]. \tag{6}$$

The dimensionless radial and transverse velocity components (u, v) can be obtained using

$$u = -\frac{1}{M}\frac{\partial\psi}{\partial\theta}, \quad v = \frac{1}{M}\frac{\partial\psi}{\partial\xi}, \tag{7}$$

and the vorticity is related to these velocity components by

$$\zeta = \frac{1}{M^2}\left[\frac{\partial}{\partial\xi}(Mv) - \frac{\partial}{\partial\theta}(Mu)\right]. \tag{8}$$

The surface boundary conditions include the impermeability and Navier slip conditions (according to Beavers and Joseph [1]) given by

$$u = 0, \quad v = \beta\frac{\partial v}{\partial\xi} \quad \text{at} \quad \xi = 0,$$

respectively. The parameter β denotes the dimensionless slip length which is related to the dimensional slip length β^* through $\beta = \beta^*/c$. When $\beta = 0$, this reduces to the usual no-slip condition. In terms of ψ and ζ, these conditions become

$$\psi = 0, \quad \frac{\partial\psi}{\partial\xi} = \left(\frac{\beta M_0^4}{M_0^2 + \frac{\beta}{2}\sinh(2\xi_0)}\right)\zeta \quad \text{at} \quad \xi = 0 \quad \text{where } M_0^2 = \frac{1}{2}[\cosh(2\xi_0) - \cos(2\theta)] \tag{9}$$

and correspond to the metric evaluated on the surface. In addition, we have the periodicity conditions

$$\psi(\xi, \theta, t) = \psi(\xi, \theta + 2\pi, t), \quad \zeta(\xi, \theta, t) = \zeta(\xi, \theta + 2\pi, t), \tag{10}$$

and the far-field conditions

$$\psi \to \frac{1}{2}e^{\xi+\xi_0}\sin(\theta + \alpha), \quad \zeta \to 0 \quad \text{as} \quad \xi \to \infty. \tag{11}$$

Conditions (11) are a result of the uniform oncoming flow.

The boundary conditions (9) reveal a complicated coupling between the surface vorticity and stream function gradient. As mentioned in Part 1, the integral conditions proposed by Dennis and Quartapelle [2] provide an alternative. For the geometry considered in Part 2, these conditions become

$$\int_0^\infty \int_0^{2\pi} e^{-n\xi} M^2\zeta(\xi, \theta, t)\sin(n\theta)\mathrm{d}\theta\mathrm{d}\xi = \pi e^{\xi_0}\cos\alpha\delta_{1,n}$$
$$-\beta\int_0^{2\pi}\left(\frac{M_0^4}{M_0^2 + \frac{\beta}{2}\sinh(2\xi_0)}\right)\zeta(0, \theta, t)\sin(n\theta)\mathrm{d}\theta, \quad n = 1, 2, \ldots, \tag{12}$$

$$\int_0^\infty \int_0^{2\pi} e^{-n\xi} M^2\zeta(\xi, \theta, t)\cos(n\theta)\mathrm{d}\theta\mathrm{d}\xi = \pi e^{\xi_0}\sin\alpha\delta_{1,n}$$
$$-\beta\int_0^{2\pi}\left(\frac{M_0^4}{M_0^2 + \frac{\beta}{2}\sinh(2\xi_0)}\right)\zeta(0, \theta, t)\cos(n\theta)\mathrm{d}\theta, \quad n = 0, 1, 2, \ldots, \tag{13}$$

where $\delta_{i,n}$ is the Kronecker delta, defined by

$$\delta_{i,n} = \begin{cases} 1 & \text{if } n = i \\ 0 & \text{if } n \neq i \end{cases}.$$

Later, we will explain how to determine surface vorticity using these integral constraints.

As a consequence of the impulsive start delivered to the cylinder, a thin boundary layer of thickness $\sqrt{8t/R}$ will surround the cylinder. For this reason, we stretch the coordinate ξ and flow variables according to

$$\xi = \lambda z, \quad \psi = \lambda\Psi, \quad \zeta = \omega/\lambda \quad \text{where } \lambda = \sqrt{\frac{8t}{R}}. \tag{14}$$
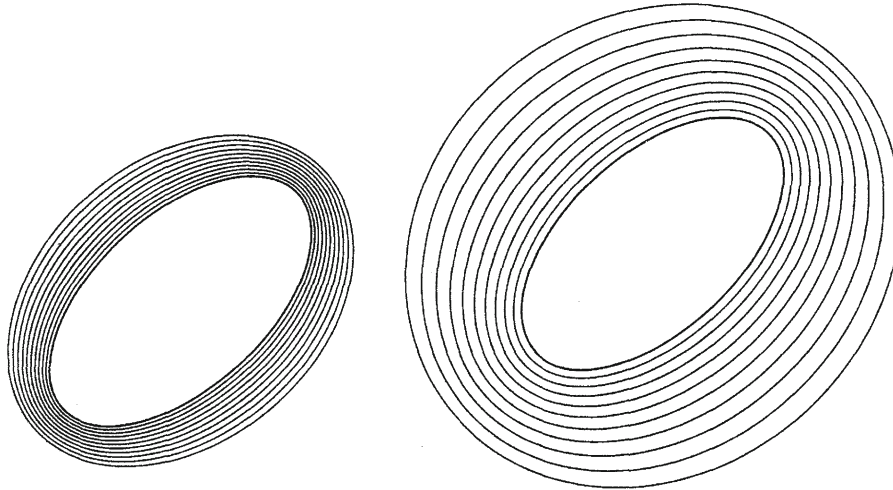
Fig. 3 Typical boundary-layer coordinates expanding with time: t_1 (left) and $t_2 > t_1$ (right)

This has the effect of removing the inherent initial singularity and also better resolving the early development of the flow. To appreciate the impact of using these so-called boundary-layer coordinates (z, θ), shown in Fig. 3 in Cartesian coordinates are lines of constant z at two different times. We see from this that the grid is alive and expands with time. This is extremely beneficial from a numerical point of view because it guarantees that we maintain adequate resolution within the growing boundary layer where the flow is changing rapidly.

In terms of the boundary-layer coordinates (z, θ), Eqs. (4)–(5) transform to

$$\frac{\partial^2 \Psi}{\partial z^2} + \lambda^2 \frac{\partial^2 \Psi}{\partial \theta^2} = M^2 \omega, \tag{15}$$

$$\frac{1}{M^2} \frac{\partial^2 \omega}{\partial z^2} + 2z \frac{\partial \omega}{\partial z} + 2\omega = 4t \frac{\partial \omega}{\partial t} - \frac{\lambda^2}{M^2} \frac{\partial^2 \omega}{\partial \theta^2} - \frac{4t}{M^2} \left(\frac{\partial \Psi}{\partial \theta} \frac{\partial \omega}{\partial z} - \frac{\partial \Psi}{\partial z} \frac{\partial \omega}{\partial \theta} \right). \tag{16}$$

These equations are to be used to solve the early stages of the flow. It is worth adding that this transformation along with the integral conditions has been successfully used in previous studies involving this geometry. For example, the study of D'Alessio' and Perera [3] adopted this approach to solve the problem of unsteady free convection from an elliptic cylinder for large Grashof numbers while Steinmoeller, D'Alessio, and Poulin [4] modified this procedure to solve the geophysical fluid mechanics problem of flow past an elliptic obstacle in the ocean.

Presented in the next Section is an analytical procedure by which we can derive an approximate solution for small times and large Reynolds numbers. As part of this process, we will obtain the exact initial solution which will be used as an initial condition for the numerical solution procedure outlined in the subsequent Section.

2 Analytical solution procedure

As in Part 1, we expand the flow variables in a double series in terms of λ and t. That is, we first expand Ψ and ω in a series of the form

$$\begin{aligned} \Psi &= \Psi_0 + \lambda \Psi_1 + \lambda^2 \Psi_2 + \cdots, \\ \omega &= \omega_0 + \lambda \omega_1 + \lambda^2 \omega_2 + \cdots, \end{aligned} \tag{17}$$

and then each $\Psi_n, \omega_n, n = 0, 1, 2, \ldots$, is further expanded in a series,

$$\begin{aligned} \Psi_n(z, \theta, t) &= \Psi_{n0}(z, \theta) + t \Psi_{n1}(z, \theta) + \cdots, \\ \omega_n(z, \theta, t) &= \omega_{n0}(z, \theta) + t \omega_{n1}(z, \theta) + \cdots. \end{aligned} \tag{18}$$

Substituting the series (17)–(18) into Eqs. (15)–(16) and using the expansions

$$M^2 = M_0^2 + \sinh(2\xi_0)\lambda z + \cosh(2\xi_0)\lambda^2 z^2 + \cdots,$$

$$e^{-n\lambda z} = 1 - n\lambda z + \frac{1}{2}n^2\lambda^2 z^2 + \cdots,$$

with M_0 given by (9), will produce a hierarchy of problems at various orders. The leading-order terms in the series, Ψ_0 and ω_0, referred to as the boundary-layer solution, satisfy

$$\frac{\partial^2 \Psi_0}{\partial z^2} = M_0^2 \omega_0, \tag{19}$$

$$\frac{1}{M_0^2}\frac{\partial^2 \omega_0}{\partial z^2} + 2z\frac{\partial \omega_0}{\partial z} + 2\omega_0 = 4t\frac{\partial \omega_0}{\partial t} - \frac{4t}{M_0^2}\left(\frac{\partial \Psi_0}{\partial \theta}\frac{\partial \omega_0}{\partial z} - \frac{\partial \Psi_0}{\partial z}\frac{\partial \omega_0}{\partial \theta}\right) \tag{20}$$

and are still too complicated to solve analytically.

To make analytical progress, we further expand (19)–(20) in powers of t. The leading-order terms in this second expansion, Ψ_{00} and ω_{00}, correspond to the initial solution at $t = 0$ and satisfy

$$\frac{\partial^2 \Psi_{00}}{\partial z^2} = M_0^2 \omega_{00}, \tag{21}$$

$$\frac{1}{M_0^2}\frac{\partial^2 \omega_{00}}{\partial z^2} + 2z\frac{\partial \omega_{00}}{\partial z} + 2\omega_{00} = 0. \tag{22}$$

It follows that the solution to (22) satisfying all the conditions is the trivial solution $\omega_{00} = 0$. Further, it can be shown that $\omega_{0n} = 0$ for $n = 1, 2, 3\ldots$. Using this result and integrating (21) twice and imposing the impermeability condition yield $\Psi_{00} = A(\theta)z$. The function $A(\theta)$ can be determined by applying the Navier slip condition which when expanded yields

$$\frac{\partial \Psi_{00}}{\partial z} = \left(\frac{\beta M_0^4}{M_0^2 + \frac{\beta}{2}\sinh(2\xi_0)}\right)\omega_{10} \quad \text{at} \quad z = 0.$$

From this, we see that in order to determine Ψ_{00}, we must first solve for ω_{10}.

The term ω_{10} satisfies the equation

$$\frac{1}{M_0^2}\frac{\partial^2 \omega_{10}}{\partial z^2} + 2z\frac{\partial \omega_{10}}{\partial z} = 0. \tag{23}$$

The solution satisfying the far-field condition $\omega_{10} \to 0$ as $z \to \infty$ is given by

$$\omega_{10}(z, \theta) = B(\theta)\mathrm{erfc}(M_0 z),$$

where $\mathrm{erfc}(z) = 1 - \mathrm{erf}(z)$ is the complementary error function and

$$\mathrm{erf}(z) = \frac{2}{\sqrt{\pi}}\int_0^z e^{-u^2}\mathrm{d}u$$

denotes the error function. In order to determine the function $B(\theta)$, the integral conditions (12)–(13) need to be enforced. Switching to boundary-layer coordinates and expanding them, the leading-order terms in (12)–(13) become

$$\beta\int_0^{2\pi}\left(\frac{M_0^4}{M_0^2 + \frac{\beta}{2}\sinh(2\xi_0)}\right)B(\theta)\sin(n\theta)\mathrm{d}\theta = \pi e^{\xi_0}\cos\alpha\,\delta_{1,n}, \quad n = 1, 2, \ldots,$$

$$\beta\int_0^{2\pi}\left(\frac{M_0^4}{M_0^2 + \frac{\beta}{2}\sinh(2\xi_0)}\right)B(\theta)\cos(n\theta)\mathrm{d}\theta = \pi e^{\xi_0}\sin\alpha\,\delta_{1,n}, \quad n = 0, 1, 2, \ldots,$$

from which it follows that

$$B(\theta) = \frac{e^{\xi_0}}{\beta}\left(\frac{M_0^2 + \frac{\beta}{2}\sinh(2\xi_0)}{M_0^4}\right)\sin(\theta + \alpha) \quad \text{and hence} \quad A(\theta) = e^{\xi_0}\sin(\theta + \alpha).$$

Thus, the leading-order nonzero terms in the solution become

$$\Psi_{00}(z,\theta) = e^{\xi_0} z \sin(\theta + \alpha), \quad \omega_{10}(z,\theta) = \frac{e^{\xi_0}}{\beta} \left(\frac{M_0^2 + \frac{\beta}{2}\sinh(2\xi_0)}{M_0^4} \right) \mathrm{erfc}(M_0 z) \sin(\theta + \alpha).$$

The leading-order solution constructed can be checked against the potential flow solution which satisfies

$$\frac{\partial^2 \psi}{\partial \xi^2} + \frac{\partial^2 \psi}{\partial \theta^2} = 0$$

subject to

$$\psi = \frac{\partial \psi}{\partial \theta} = 0 \text{ on } \xi = 0 \quad \text{and} \quad \psi \to \frac{1}{2} e^{\xi + \xi_0} \sin(\theta + \alpha) \quad \text{as} \quad \xi \to \infty.$$

The solution is easily found to be

$$\psi(\xi, \theta) = e^{\xi_0} \sinh \xi \sin(\theta + \alpha),$$

from which we obtain

$$v = \frac{1}{M} \frac{\partial \psi}{\partial \xi} = \frac{e^{\xi_0}}{M} \cosh \xi \sin(\theta + \alpha).$$

Now, in the large R limit, the transverse velocity according to our expansion becomes

$$v = \frac{1}{M_0} \frac{\partial \Psi_{00}}{\partial z} = \frac{e^{\xi_0}}{M_0} \sin(\theta + \alpha).$$

Evaluating this in the limit as $z \to \infty$, we see that it is in full agreement with the corresponding potential flow expression when evaluated on the surface $\xi = 0$.

Continuing the procedure and solving for the next terms, Ψ_{10} and ω_{20}, in the series we find that ω_{20} satisfies

$$\frac{\partial^2 \omega_{20}}{\partial s^2} + 2s \frac{\partial \omega_{20}}{\partial s} - 2\omega_{20} = -\frac{2\sinh(2\xi_0)}{M_0^3} s^2 \frac{\partial \omega_{10}}{\partial s} \tag{24}$$

and must obey the far-field condition $\omega_{20} \to 0$ as $s \to \infty$. Here, we have made the change of variable $s = M_0 z$. The solution for $\omega_{20}(s, \theta)$ obeying the far-field condition has been found to be

$$\omega_{20}(s, \theta) = C(\theta)(e^{-s^2} - \sqrt{\pi} s \mathrm{erfc}(s)) - \frac{\sinh(2\xi_0) B(\theta)}{4M_0^3} \left(s \mathrm{erfc}(s) + \frac{2}{\sqrt{\pi}} s^2 e^{-s^2} \right).$$

The unknown function $C(\theta)$ must be determined by imposing the integral conditions given by

$$\beta \int_0^{2\pi} \left(\frac{M_0^4}{M_0^2 + \frac{\beta}{2}\sinh(2\xi_0)} \right) \omega_{20}(0, \theta) \sin(n\theta) \mathrm{d}\theta = -\int_0^\infty \int_0^{2\pi} M_0 \omega_{10}(s, \theta) \sin(n\theta) \mathrm{d}\theta \mathrm{d}s,$$

for $n = 1, 2, \ldots,$ and

$$\beta \int_0^{2\pi} \left(\frac{M_0^4}{M_0^2 + \frac{\beta}{2}\sinh(2\xi_0)} \right) \omega_{20}(0, \theta) \cos(n\theta) \mathrm{d}\theta = -\int_0^\infty \int_0^{2\pi} M_0 \omega_{10}(s, \theta) \cos(n\theta) \mathrm{d}\theta \mathrm{d}s,$$

for $n = 0, 1, 2, \ldots.$ It follows that $C(\theta)$ is given by

$$C(\theta) = -\frac{M_0 e^{\xi_0}}{\sqrt{\pi} \beta^2} \left(\frac{M_0^2 + \frac{\beta}{2}\sinh(2\xi_0)}{M_0^4} \right)^2 \sin(\theta + \alpha).$$

The solution for $\Psi_{10}(s, \theta)$ can be easily found by integrating

$$\frac{\partial^2 \Psi_{10}}{\partial s^2} = \omega_{10} \tag{25}$$

twice and imposing the conditions

$$\Psi_{10} = 0, \quad \frac{\partial \Psi_{10}}{\partial s} = \left(\frac{\beta M_0^3}{M_0^2 + \frac{\beta}{2}\sinh(2\xi_0)}\right)\omega_{20} \text{ at } s = 0.$$

The resulting solution for Ψ_{10} is given by

$$\Psi_{10}(s, \theta) = \frac{e^{\xi_0}}{\beta}\left(\frac{M_0^2 + \frac{\beta}{2}\sinh(2\xi_0)}{M_0^4}\right)\left(\frac{s^2}{2}\text{erfc}(s) - \frac{1}{4}\text{erf}(s) - \frac{s}{2\sqrt{\pi}}e^{-s^2}\right)\sin(\theta + \alpha) .$$

In summary, we have the approximate solution given by

$$\Psi \sim \Psi_{00} + \lambda\Psi_{10}, \quad \omega \sim \lambda\,\omega_{10} + \lambda^2\,\omega_{20}.$$

Later, this solution will be used to validate the numerical solution which is described in the next Section.

3 Numerical solution procedure

Although the numerical method used to solve Eqs. (15)–(16) is identical to that discussed in Part 1, there are some subtleties that arise as a result of the geometry which will be explained. Before proceeding to outline the scheme, we first discretize the computational domain bounded by $0 \leq z \leq z_\infty$ into L equally spaced grid points located at

$$z_j = j\Delta z, \quad j = 0, 1, \ldots, L, \tag{26}$$

where $\Delta z = z_\infty/L$ and z_∞ denotes the outer boundary approximating infinity.

The flow variables (Ψ, ω) are next expanded in the truncated Fourier series

$$\Psi = \frac{F_0(z, t)}{2} + \sum_{n=1}^{N}[F_n(z, t)\cos(n\theta) + f_n(z, t)\sin(n\theta)], \tag{27}$$

$$\omega = \frac{G_0(z, t)}{2} + \sum_{n=1}^{N}[G_n(z, t)\cos(n\theta) + g_n(z, t)\sin(n\theta)]. \tag{28}$$

Substituting these series into (15)–(16) yields the following system of $4N + 2$ equations for the Fourier coefficients:

$$\frac{\partial^2 F_0}{\partial z^2} = \frac{1}{2}\left(\cosh[2(\lambda z + \xi_0)]G_0 - G_2\right), \tag{29}$$

$$\frac{\partial^2 F_n}{\partial z^2} - (n\lambda)^2 F_n = \frac{1}{2}\cosh[2(\lambda z + \xi_0)]G_n - \frac{1}{4}(G_{n+2} + G_{|n-2|}), \tag{30}$$

$$\frac{\partial^2 f_n}{\partial z^2} - (n\lambda)^2 f_n = \frac{1}{2}\cosh[2(\lambda z + \xi_0)]g_n - \frac{1}{4}(g_{n+2} + \text{sgn}(n-2)g_{|n-2|}) \tag{31}$$

where $n = 1, 2, \ldots, N$, and

$$\frac{\partial^2 G_0}{\partial z^2} + \cosh[2(\lambda z + \xi_0)]\left(z\frac{\partial G_0}{\partial z} + G_0\right)$$
$$= 2t\cosh[2(\lambda z + \xi_0)]\frac{\partial G_0}{\partial t} - 2t\frac{\partial G_2}{\partial t} + z\frac{\partial G_2}{\partial z} + G_2 - 4tS_0, \tag{32}$$

$$\frac{\partial^2 G_1}{\partial z^2} + \cosh[2(\lambda z + \xi_0)]z\frac{\partial G_1}{\partial z} + (\cosh[2(\lambda z + \xi_0)] - \lambda^2)G_1$$

$$= -t\left(\frac{\partial G_3}{\partial t} + \frac{\partial G_1}{\partial t}\right) + \frac{z}{2}\left(\frac{\partial G_3}{\partial z} + \frac{\partial G_1}{\partial z}\right)$$

$$+ 2t\cosh[2(\lambda z + \xi_0)]\frac{\partial G_1}{\partial t} + \frac{1}{2}(G_3 + G_1) - 2t S_1, \tag{33}$$

$$\frac{\partial^2 G_n}{\partial z^2} + \cosh[2(\lambda z + \xi_0)]z\frac{\partial G_n}{\partial z} + (\cosh[2(\lambda z + \xi_0)] - (n\lambda)^2)G_n$$

$$= -t\left(\frac{\partial G_{n+2}}{\partial t} + \frac{\partial G_{|n-2|}}{\partial t}\right) + \frac{z}{2}\left(\frac{\partial G_{n+2}}{\partial z} + \frac{\partial G_{|n-2|}}{\partial z}\right)$$

$$+ 2t\cosh[2(\lambda z + \xi_0)]\frac{\partial G_n}{\partial t} + \frac{1}{2}(G_{n+2} + G_{|n-2|}) - 2t S_n, \tag{34}$$

$$\frac{\partial^2 g_1}{\partial z^2} + \cosh[2(\lambda z + \xi_0)]z\frac{\partial g_1}{\partial z} + (\cosh[2(\lambda z + \xi_0)] - \lambda^2)g_1 = \frac{z}{2}\left(\frac{\partial g_3}{\partial z} - \frac{\partial g_1}{\partial z}\right)$$

$$- t\left(\frac{\partial g_3}{\partial t} - \frac{\partial g_1}{\partial t}\right) + 2t\cosh[2(\lambda z + \xi_0)]\frac{\partial g_1}{\partial t} + \frac{1}{2}(g_3 - g_1) - 2t T_1, \tag{35}$$

$$\frac{\partial^2 g_n}{\partial z^2} + \cosh[2(\lambda z + \xi_0)]z\frac{\partial g_n}{\partial z} + (\cosh[2(\lambda z + \xi_0)] - (n\lambda)^2)g_n$$

$$= \frac{z}{2}\left(\frac{\partial g_{n+2}}{\partial z} + \text{sgn}(n-2)\frac{\partial g_{|n-2|}}{\partial z}\right) - t\left(\frac{\partial g_{n+2}}{\partial t} + \text{sgn}(n-2)\frac{\partial g_{|n-2|}}{\partial t}\right)$$

$$+ 2t\cosh[2(\lambda z + \xi_0)]\frac{\partial g_n}{\partial t} + \frac{1}{2}(g_{n+2} + \text{sgn}(n-2)g_{|n-2|}) - 2t T_n \tag{36}$$

where $\text{sgn}(m)$ denotes the sign of m with $\text{sgn}(0) = 0$, and $n = 2, 3, \ldots, N$. The quantities S_0, S_n, T_n represent nonlinear terms and are given by

$$S_0 = \sum_{n=1}^{N} \frac{\partial}{\partial z}[n(f_n G_n - F_n g_n)], \tag{37}$$

$$S_n = \sum_{m=1}^{N}\left(\frac{\partial G_m}{\partial z}[(m+n)f_{m+n} + |m-n|f_{|m-n|}]\right.$$

$$+ mG_m\left[\frac{\partial f_{m+n}}{\partial z} + \text{sgn}(m-n)\frac{\partial f_{|m-n|}}{\partial z}\right]$$

$$- mg_m\left[\frac{\partial F_{m+n}}{\partial z} + \frac{\partial F_{|m-n|}}{\partial z}\right]$$

$$\left.- \frac{\partial g_m}{\partial z}[(m+n)F_{m+n} + (m-n)F_{|m-n|}]\right)$$

$$+ nf_n\frac{\partial G_0}{\partial z} - ng_n\frac{\partial F_0}{\partial z}, \tag{38}$$

$$T_n = \sum_{m=1}^{N}\left(\frac{\partial g_m}{\partial z}[|m-n|f_{|m-n|} - (m+n)f_{m+n}]\right.$$

$$- mG_m\left[\frac{\partial F_{m+n}}{\partial z} - \frac{\partial F_{|m-n|}}{\partial z}\right]$$

$$- mg_m\left[\frac{\partial f_{m+n}}{\partial z} - \text{sgn}(m-n)\frac{\partial f_{|m-n|}}{\partial z}\right]$$

$$\left.- \frac{\partial G_m}{\partial z}[(m+n)F_{m+n} - (m-n)F_{|m-n|}]\right)$$

$$+ nG_n\frac{\partial F_0}{\partial z} - nF_n\frac{\partial G_0}{\partial z}. \tag{39}$$

We first discuss the procedure for solving for the vorticity. This requires solving (32)–(36) subject to the far-field condition (11) which, in terms of the Fourier coefficients, becomes

$$G_n, \; g_n \to 0 \text{ as } z \to \infty, \tag{40}$$

for $n = 0, 1, 2, \ldots, N$. Rewriting the integral conditions in terms of the boundary-layer coordinate z and the Fourier coefficients G_0, G_n, g_n yields

$$\int_0^\infty (\cosh[2(\lambda z + \xi_0)]G_0 - G_2)\mathrm{d}z = -\frac{\beta K_1}{\lambda} G_0(0, t) + \frac{\beta}{\lambda} G_2(0, t)$$
$$-\frac{\beta^3 \sinh^2(2\xi_0)}{\pi \lambda} \int_0^{2\pi} \frac{\omega(0, \theta, t)\mathrm{d}\theta}{K_2 - \cos(2\theta)}, \tag{41}$$

$$\int_0^\infty e^{-n\lambda z}(2\cosh[2(\lambda z + \xi_0)]G_n - G_{|n-2|} - G_{n+2})\mathrm{d}z = 4e^{\xi_0}\sin\alpha\,\delta_{1,n} - \frac{2\beta K_1}{\lambda} G_n(0, t)$$
$$+\frac{\beta}{\lambda}\left(G_{|n-2|}(0, t) + G_{n+2}(0, t)\right) - \frac{2\beta^3 \sinh^2(2\xi_0)}{\pi \lambda} \int_0^{2\pi} \frac{\omega(0, \theta, t)\cos(n\theta)\mathrm{d}\theta}{K_2 - \cos(2\theta)}, \tag{42}$$

$$\int_0^\infty e^{-n\lambda z}(2\cosh[2(\lambda z + \xi_0)]g_n - \mathrm{sgn}(n-2)g_{|n-2|} - g_{n+2})\mathrm{d}z = 4e^{\xi_0}\cos\alpha\,\delta_{1,n} - \frac{2\beta K_1}{\lambda} g_n(0, t)$$
$$+\frac{\beta}{\lambda}\left(\mathrm{sgn}(n-2)g_{|n-2|}(0, t) + g_{n+2}(0, t)\right) - \frac{2\beta^3 \sinh^2(2\xi_0)}{\pi \lambda} \int_0^{2\pi} \frac{\omega(0, \theta, t)\sin(n\theta)\mathrm{d}\theta}{K_2 - \cos(2\theta)}, \tag{43}$$

for $n = 1, 2, 3, \ldots$, where

$$K_1 = \cosh(2\xi_0) - \beta \sinh(2\xi_0), \;\; K_2 = \cosh(2\xi_0) + \beta \sinh(2\xi_0).$$

For simplicity, we illustrate the numerical method using Eq. (32) with the understanding that (33)–(36) are solved in a similar manner. Equation (32) may be rewritten in the generic form

$$2t\frac{\partial G_0}{\partial t} - \frac{2t}{\cosh[2(\lambda z + \xi_0)]}\frac{\partial G_2}{\partial t} = Q(z, t) \tag{44}$$

where

$$Q(z, t) = \frac{1}{\cosh[2(\lambda z + \xi_0)]}\frac{\partial^2 G_0}{\partial z^2} + z\frac{\partial G_0}{\partial z} + G_0$$
$$+\frac{1}{\cosh[2(\lambda z + \xi_0)]}\left(z\frac{\partial G_2}{\partial z} + G_2\right) + \frac{4t}{\cosh[2(\lambda z + \xi_0)]}S_0. \tag{45}$$

Assuming the solution at time t is known, we can advance the solution to time $t + \Delta t$ by integrating Eq. (44). Integration by parts yields

$$2\tau G_0\big|_t^{t+\Delta t} - 2\int_t^{t+\Delta t} G_0\mathrm{d}\tau - \frac{2}{\cosh[2(\lambda z + \xi_0)]}(\tau G_2)\big|_t^{t+\Delta t}$$
$$-\frac{2}{\cosh[2(\lambda z + \xi_0)]}\int_t^{t+\Delta t} G_2\mathrm{d}\tau = \int_t^{t+\Delta t} Q\mathrm{d}\tau \tag{46}$$

where Δt is the time increment. In arriving at (46), we have made the reasonable approximation of treating $\cosh[2(\lambda z + \xi_0)]$ as a constant over the time increment. We now approximate the integrals using

$$\int_t^{t+\Delta t} \chi\mathrm{d}\tau \approx \Delta t[\varpi \chi(z, t + \Delta t) + (1 - \varpi)\chi(z, t)] \tag{47}$$

where ϖ is a weight factor and χ is a generic function. In general, $0 \le \varpi \le 1$, and we treat ϖ as a computational parameter still to be specified. When $\varpi = 1/2$, we obtain the well-known Crank–Nicolson scheme while $\varpi = 1$ yields the fully implicit scheme. The case $\varpi = 0$ corresponds to an explicit scheme which will not be considered.

With this approximation in place, Eq. (46) brings us to the expression

$$2[t + (1 - \varpi)\Delta t](G_0(z, t + \Delta t) - G_0(z, t))$$
$$- \frac{2}{\cosh[2(\lambda z + \xi_0)]}[t + (1 - \varpi)\Delta t](G_2(z, t + \Delta t) - G_2(z, t))$$
$$= \Delta t[\varpi Q(z, t + \Delta t) + (1 - \varpi)Q(z, t)]. \tag{48}$$

We next substitute $Q(z, t + \Delta t)$ given by (45) into (48) and replace all spatial derivatives by central differences at the point z. Now (48) can be written in the form

$$C_1(z, t + \Delta t)G_0(z - \Delta z, t + \Delta t) + C_2(z, t + \Delta t)G_0(z, t + \Delta t)$$
$$+ C_3(z, t + \Delta t)G_0(z + \Delta z, t + \Delta t) = D(z, t + \Delta t) + E(z, t). \tag{49}$$

The functions C_1, C_2, C_3, D, E can be easily obtained and do not involve G_0. The function E is known from the previous time step while the functions C_1, C_2, C_3, D are computed using the most recent available information as an initial guess. Thus, when represented in matrix form, Eq. (49) becomes a tri-diagonal system for the unknown values of G_0 at the grid points $z = 0, \Delta z, 2\Delta z, \ldots$. When the region $0 \leq z \leq z_\infty$ is divided into L equally spaced intervals of Δz, an $(L - 1) \times (L - 1)$ tri-diagonal matrix is resulting.

At each time step, we need to solve this system subject to the far-field condition $G_0(z_\infty, t + \Delta t) = 0$ and the integral condition given by (41). To enforce the integral constraint, we proceed as follows. First, we obtain the homogeneous solution, G_0^h, by setting the right-hand side in (49) to zero, with G_0^h satisfying $G_0^h(0, t + \Delta t) = 1$ and $G_0^h(z_\infty, t + \Delta t) = 0$. Then, we find the particular solution G_0^p to (49) again satisfying $G_0^p(0, t + \Delta t) = 1$ and $G_0^p(z_\infty, t + \Delta t) = 0$. We form the complete solution as

$$G_0(z, t + \Delta t) = \gamma G_0^h(z, t + \Delta t) + G_0^p(z, t + \Delta t). \tag{50}$$

Plugging the decomposition (50) into the integral condition (41) and solving for γ yields $\gamma = $ Num/Denom where

$$\text{Num} = -\int_0^{z_\infty} (\cosh[2(\lambda z + \xi_0)]G_0^p - G_2)\mathrm{d}z - \frac{\beta}{\lambda}(K_1 - G_2(0, t)) - \frac{\beta^3 \sinh^2(2\xi_0)}{\lambda\sqrt{K_2^2 - 1}}$$

$$- \frac{\beta^3 \sinh^2(2\xi_0)}{\pi\lambda} \sum_{n=1}^{N/2} \int_0^{2\pi} \frac{G_{2n}(0, t)\cos(2n\theta)\mathrm{d}\theta}{K_2 - \cos(2\theta)},$$

$$\text{Denom} = \int_0^{z_\infty} \cosh[2(\lambda z + \xi_0)]G_0^h\mathrm{d}z + \frac{\beta K_1}{\lambda} + \frac{\beta^3 \sinh^2(2\xi_0)}{\lambda\sqrt{K_2^2 - 1}}.$$

In arriving at this expression, we have made use of

$$\int_0^{2\pi} \frac{\omega(0, \theta, t)\mathrm{d}\theta}{K_2 - \cos(2\theta)} = \frac{\pi G_0(0, t)}{\sqrt{K_2^2 - 1}} + \sum_{n=1}^{N/2} \int_0^{2\pi} \frac{G_{2n}(0, t)\cos(2n\theta)\mathrm{d}\theta}{K_2 - \cos(2\theta)},$$

since

$$\int_0^{2\pi} \frac{\sin(n\theta)\mathrm{d}\theta}{K_2 - \cos(2\theta)} = \int_0^{2\pi} \frac{\cos[(2n + 1)\theta]\mathrm{d}\theta}{K_2 - \cos(2\theta)} = 0,$$

for $n = 1, 2, 3, \ldots$, and

$$\int_0^{2\pi} \frac{\mathrm{d}\theta}{K_2 - \cos(2\theta)} = \frac{2\pi}{\sqrt{K_2^2 - 1}}.$$

The integrals appearing in the above are computed using Simpson's rule. An efficient solver is implemented to solve the tri-diagonal systems for G_0^h and G_0^p. With our approximate solution to $G_0(z, t + \Delta t)$ now found, we then repeat this procedure for obtaining approximate solutions to $G_n(z, t + \Delta t), g_n(z, t + \Delta t)$ for $n =$

$1, 2, \ldots, N$. It must be remembered that when solving for G_n or g_n, quantities having a subscript larger than n (such as $n + 2$) are unknown and therefore must be approximated using the values at the previous time step and then continuously update their values during the iterative procedure. Further, whenever the subscript $n + 2$ of a quantity exceeds N, the value taken by that quantity is zero.

The method used here to solve (29)–(31) for the stream function is identical to that outlined in Dennis and Chang [5] and will be briefly described. First, the right-hand sides of these equations are obtained using the computed solutions G_0, G_n, g_n for $n = 1, 2, \ldots, N$. These stream function coefficient equations are then integrated using stable marching algorithms satisfying the Navier slip and impermeability conditions at $z = 0$

$$F_0 = F_n = f_n = 0,$$

$$\frac{\partial F_0}{\partial z} = \frac{4\lambda}{a_1} \frac{\partial F_2}{\partial z} + \frac{a_2}{a_1} G_0 - \frac{a_3}{a_1} G_2 + \frac{\beta}{a_1} G_4,$$

$$\frac{\partial F_n}{\partial z} = \frac{2\lambda}{a_1} \left(\frac{\partial F_{|n-2|}}{\partial z} + \frac{\partial F_{n+2}}{\partial z} \right) + \frac{a_2}{a_1} G_n - \frac{a_3}{2a_1} \left(G_{|n-2|} + G_{n+2} \right) + \frac{\beta}{2a_1} \left(G_{|n-4|} + G_{n+4} \right),$$

$$\frac{\partial f_n}{\partial z} = \frac{2\lambda}{a_1} \left(\text{sgn}(n-2) \frac{\partial f_{|n-2|}}{\partial z} + \frac{\partial f_{n+2}}{\partial z} \right) + \frac{a_2}{a_1} g_n$$

$$- \frac{a_3}{2a_1} \left(\text{sgn}(n-2) g_{|n-2|} + g_{n+2} \right) + \frac{\beta}{2a_1} \left(\text{sgn}(n-4) g_{|n-4|} + g_{n+4} \right)$$

where

$$a_1 = 4\lambda[\cosh(2\xi_0) + \beta \sinh(2\xi_0)], \quad a_2 = \beta[1 + 2\cosh^2(2\xi_0)], \quad a_3 = 4\beta \cosh(2\xi_0),$$

and the far-field conditions

$$F_0 \to 0 \quad \text{as } z \to \infty, \tag{51}$$

$$F_n \to -\frac{1}{2\lambda} e^{\xi_0 + \lambda z} \sin \alpha \, \delta_{1,n} \quad \text{as } z \to \infty, \tag{52}$$

$$f_n \to -\frac{1}{2\lambda} e^{\xi_0 + \lambda z} \cos \alpha \, \delta_{1,n} \quad \text{as } z \to \infty, \tag{53}$$

for $n = 1, 2, \ldots, N$. The marching algorithms used are identical to those presented in Part 1.

The entire cycle described above is repeated until convergence is reached. The convergence criterion adopted is given by

$$|G_0^{(k+1)}(z, t + \Delta t) - G_0^{(k)}(z, t + \Delta t)| < \varepsilon, \quad |G_n^{(k+1)}(z, t + \Delta t) - G_n^{(k)}(z, t + \Delta t)| < \varepsilon,$$
$$\text{and } |g_n^{(k+1)}(z, t + \Delta t) - g_n^{(k)}(z, t + \Delta t)| < \varepsilon \quad \text{for } n = 1, 2, \ldots, N.$$

Here, the superscripts k, $k + 1$ refer to two successive iterations in the cyclic procedure, and ε is some specified tolerance. To initiate the integration procedure, we use the solution at $t = 0$ given by Ψ_{00} and ω_{00} which when expressed in terms of the Fourier coefficients become

$$G_0(z, 0) = G_n(z, 0) = g_n(z, 0) = 0,$$
$$F_0(z, 0) = 0, \quad F_1(z, 0) = z e^{\xi_0} \sin \alpha, \quad F_n(z, 0) = 0, \quad f_1(z, 0) = z e^{\xi_0} \cos \alpha, \quad f_n(z, 0) = 0,$$

for $n = 2, 3, \ldots, N$.

Presented in the next Section are analytical and numerical results along with various comparisons.

4 Results and comparisons

The flow is completely characterized by the Reynolds number, R, the slip length, β, the inclination, α, and the aspect ratio, r. To confirm numerical convergence, numerous numerical experiments were carried out with different grids and time steps. From our numerical experiments, the following values for the computational parameters were used: $z_\infty = 10$, $N = 25$, $\Delta z = 0.05$ and $\varepsilon = 10^{-6}$. We have decided to run the scheme in fully implicit mode ($\varpi = 1$). Running in Crank–Nicolson mode ($\varpi = 1/2$) exhibited similar convergence

Table 1 Comparison in C_D between unsteady present and previous steady-state no-slip results for the case $\alpha = 0°$, $r = 0.2$, and Reynolds numbers $R = 20, 40$

R	Dennis and Young [8] (steady state) C_D	Present (unsteady, $t = 30$) C_D
20	0.789	0.806
40	1.228	1.224

Table 2 Comparison in C_D, C_L between unsteady present and previous steady-state no-slip results for the case $R = 20$, $r = 0.2$ and inclinations $\alpha = 20°, 40°, 60°$

α	Dennis and Young [8] (steady)		D'Alessio and Dennis [7] (steady)		Present (unsteady, $t = 10$)	
	C_D	C_L	C_D	C_L	C_D	C_L
20°	1.296	0.741	1.305	0.751	1.382	0.737
40°	1.602	0.947	1.620	0.949	1.786	0.985
60°	1.911	0.706	1.931	0.706	2.228	0.748

characteristics; however, it produced oscillations in the drag and lift coefficients for a brief time after start-up, which is a signature of the Crank–Nicolson scheme. Initial time steps of 10^{-4} were used for the first 10 advances. Then, the next ten time steps were proceeded with $\Delta t = 10^{-3}$ and continued after with $\Delta t = 0.01$. At $t = 1$, the time step was increased to $\Delta t = 0.05$. Unlike the symmetric case in Part 1 where no stability difficulties were encountered, we have observed numerical stability challenges for some of the asymmetrical cases considered. In particular, we have noticed difficulties when $r \leq 0.2$ for $\beta \neq 0$.

Of particular importance is the determination of the drag and lift coefficients, C_D and C_L, respectively, and their variation with time. The dimensionless drag and lift coefficients are derived in the "Appendix" and were computed using formula (A12). We note that for the no-slip case only the first two terms in (A10) and (A11) survive. The numerical scheme was first tested by setting $\beta = 0$ (i.e., no-slip) and comparing the drag and lift coefficients with those reported in previous studies [6–8]. We begin with the small Reynolds number symmetric case having $\alpha = 0°$ and $r = 0.2$. Contrasted in Table 1 are drag coefficients with previous steady-state results. Since we are solving the unsteady equations, time-stepping was carried out to $t = 30$, when the flow has settled down appreciably. As expected, C_L was numerically found to be zero to within our specified tolerance ε.

In Table 2, comparisons are made for the no-slip asymmetrical case having $r = 0.2$, $R = 20$, and inclinations of $\alpha = 20°, 40°, 60°$ against documented steady-state results. Full agreement could not be demonstrated because time-stepping was not carried out to large times. Here, time-stepping terminated at $t = 10$ since numerical instabilities set in beyond that. We speculate that the numerical instabilities may be due to the fact that the boundary-layer coordinate is not suitable for larger t when R is small. Although this was not done, results for larger times could be obtained by switching back to the physical coordinates (ξ, θ) and solving Eqs. (4)–(5) instead of (15)–(16). The optimal time to make the switch would be when the parameter $\lambda = \sqrt{8t/R} = 1$ since $\xi = z$ at that moment. For $R = 20$, this occurs at $t = 2.5$.

We now make a comparison for the large Reynolds number no-slip case having $R = 6250$, $r = 0.6$, $\alpha = 15°$ with the unsteady results of Staniforth [6]. Figure 4 compares the time variation of both the drag and lift coefficients. As in Part 1, we have plotted the absolute value of C_D. A discrepancy is observed in these time variations, and we think that this is due to the fact that because of the impulsive start C_D and C_L are infinite at $t = 0$, and one set of results may be better resolving this singular behavior than the other.

Another check was conducted by comparing the computed surface vorticity distribution with that predicted by our approximate analytical solution for small times. Using the analytical solution derived in Sect. 2 for the vorticity, the following expression for the surface vorticity, $\zeta(0, \theta, t)$, can be obtained:
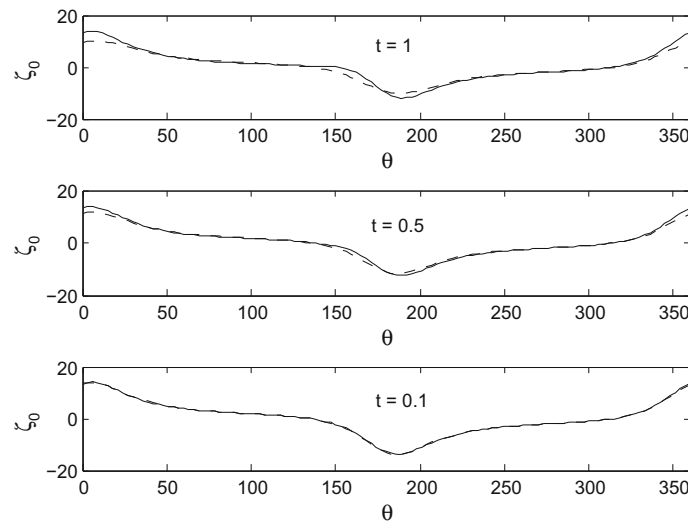
$$\zeta(0, \theta, t) \sim \frac{e^{\xi_0}}{\beta}\left(\frac{M_0^2 + \frac{\beta}{2}\sinh(2\xi_0)}{M_0^4}\right)\left[1 - \frac{\lambda M_0}{\sqrt{\pi}\beta}\left(\frac{M_0^2 + \frac{\beta}{2}\sinh(2\xi_0)}{M_0^4}\right)\right]\sin(\theta + \alpha)$$

where, as previously defined, the function $M_0(\theta)$ is given by

$$M_0^2 = \frac{1}{2}[\cosh(2\xi_0) - \cos(2\theta)].$$
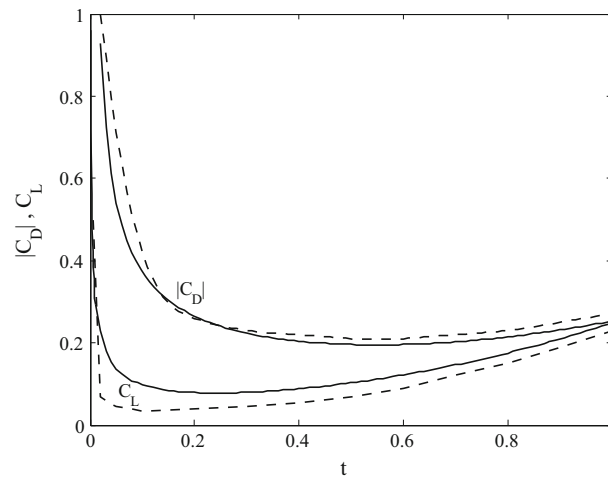
Fig. 4 Comparison in $|C_D|$, C_L between present (solid line) and Staniforth [6] (dashed line) no-slip results for the case $R = 6250$, $r = 0.6$, and $\alpha = 15°$


Fig. 5 Numerical (solid line) and analytical (dashed line) surface vorticity distributions for $R = 1000$, $\beta = 0.5$, $\alpha = 45°$, and $r = 0.5$ at various times

Contrasted in Fig. 5 are surface vorticity distributions at times $t = 0.1, 0.5, 1$ for the case $R = 1000$, $\beta = 0.5$, $\alpha = 45°$, and $r = 0.5$. As observed for the case of a circular cylinder in Part 1, the agreement between the numerical and analytical results is excellent for small times and worsens as time progresses. Of course, if more terms in the expansion were retained, then the agreement would persist for a slightly longer time. We note that the largest discrepancy occurs at the tips of the ellipse. This is to be expected since the vorticity variation is most rapid in the vicinity of the tips. For the elliptic cylinder, the general trend is that the agreement improves as R, β, and r increase.

We next consider the case with $R = 500$, $r = 0.5$, and $\alpha = 45°$. We present the no-slip case (i.e., $\beta = 0$) first to establish a baseline as a basis for comparison. Shown in Fig. 6 are instantaneous snapshots of the flow at selected times in the interval $0 < t \leq 10$ which serve to illustrate the vortex-shedding process. We see the first sign of vortex formation taking place between $t = 0.65$ and $t = 0.75$. At $t = 1$, the vortex is shed and carried downstream. This process then continues; for example, at $t = 3$, another vortex is formed while at $t = 5$ it is just starting to detach from the rear of the cylinder. The next formed vortex is seen at $t = 9$ and separates from the cylinder at $t = 10$. With time, the formed vortices grow in size and then eventually shed. As the vortices are advected downstream, they weaken and are shown as wavy streamlines. The vortex-shedding process has a significant impact on the drag and lift coefficients, which are illustrated in Fig. 7 over the interval $0 < t \leq 15$.
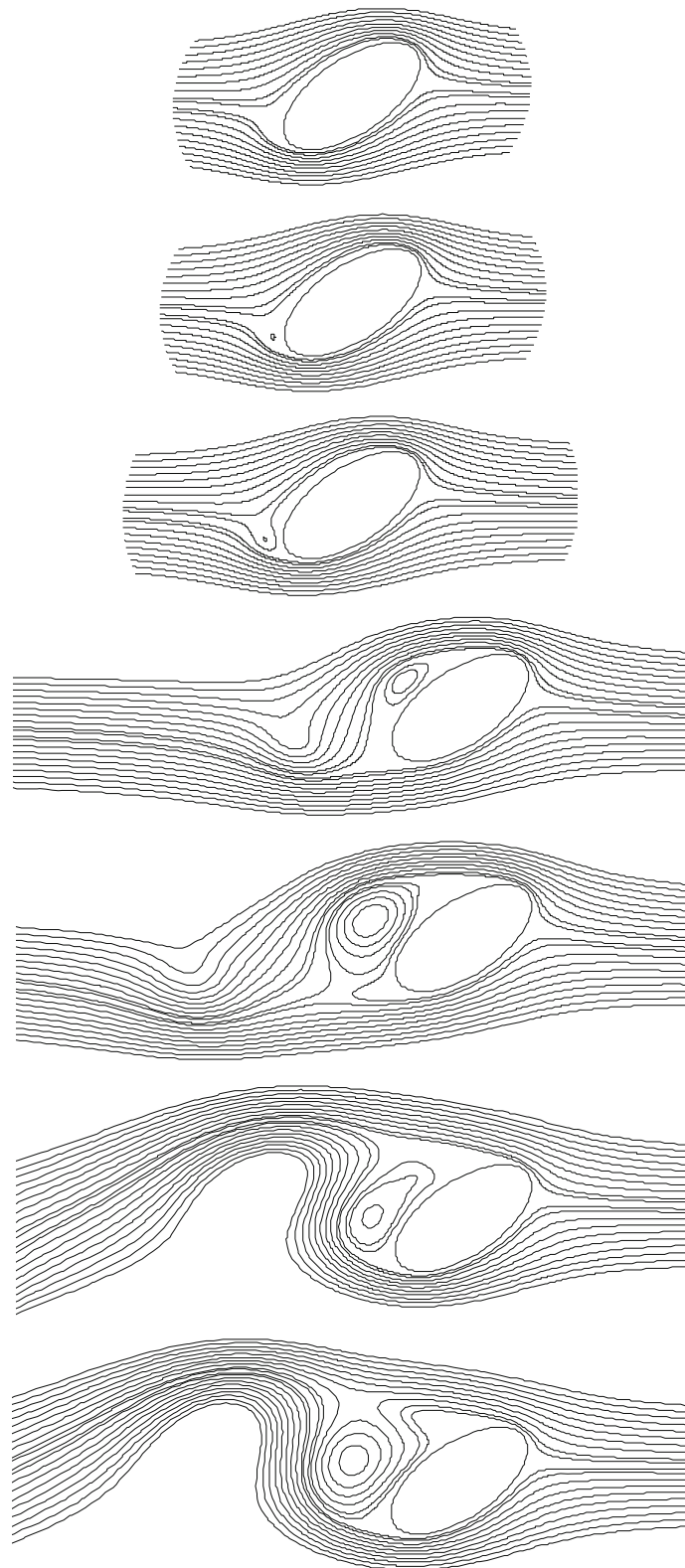
Fig. 6 Streamline plots for $R = 500, r = 0.5, \alpha = 45°$, and $\beta = 0$ at selected times $t = 0.65, 0.75, 1, 3, 5, 9, 10$ from top to bottom, respectively
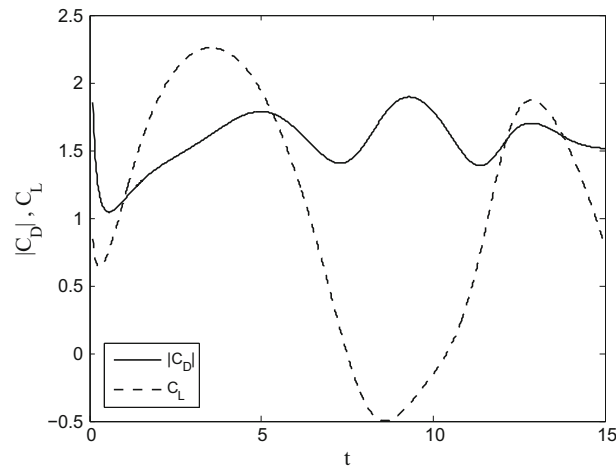
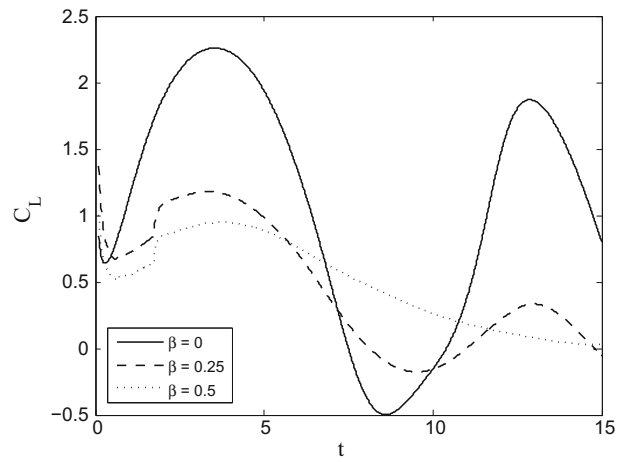**Fig. 7** Time variation in $|C_D|$, C_L for the case $R = 500$, $r = 0.5$, $\alpha = 45°$, and $\beta = 0$
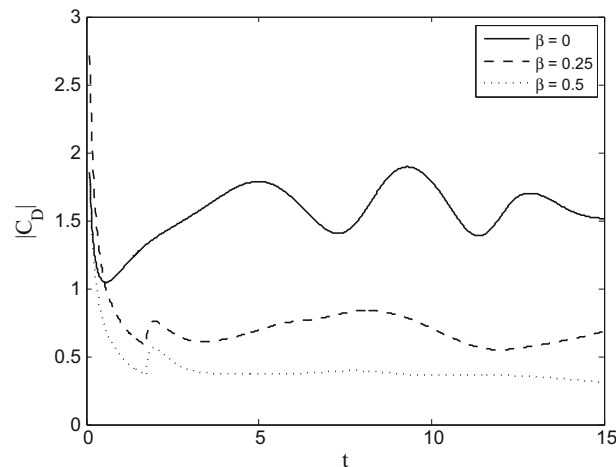
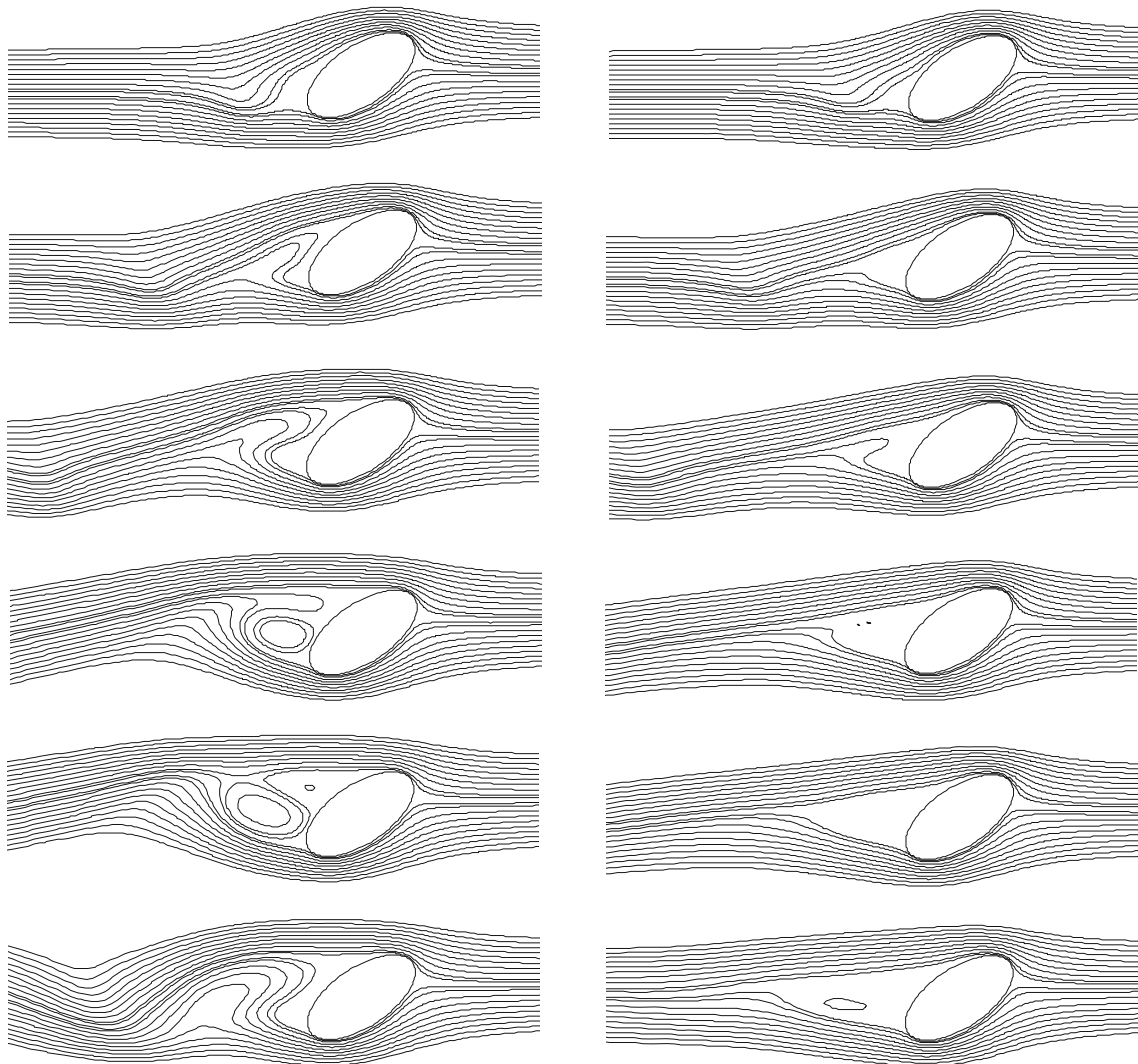**Fig. 8** Time variation in $|C_D|$ for the cases $R = 500$, $r = 0.5$, $\alpha = 45°$, and $\beta = 0, 0.25, 0.5$

Fluctuations in C_D, C_L are clearly visible, and the frequency of the oscillations in C_L appears to be about half of the frequency of the oscillations in C_D. In addition, the oscillations in C_L are more pronounced than those in C_D, and what is most striking is that $C_L < 0$ for a brief period.

We now present results for the corresponding slip case. The situation is dramatically different when compared to the no-slip case. As β increases, vortex shedding gets more suppressed. This is best illustrated by contrasting time variations of the drag and lift coefficients shown in Figs. 8 and 9, respectively. We see a significant reduction in the amplitude of oscillation in both C_D and C_L as β increases. In fact, when $\beta = 0.5$, we see no oscillations in C_D. The frequency of the oscillations also appears to be affected as β increases. More importantly, there is a noticeable reduction in drag as the slip length increases, as observed with the circular cylinder. The suppression in vortex shedding is clearly illustrated in the streamline plots shown in Fig. 10, where we contrast the cases $\beta = 0.25$ and $\beta = 0.5$; there is no sign of vortex shedding prior to $t = 3$. Another feature associated with the slip condition is apparent in the surface vorticity distribution displayed in Fig. 11. As β increases, there is less variation in ζ_0. This is especially evident in the vicinity of the tips of the cylinder. Computations were also repeated for $R = 1000$, and similar findings were observed. Figures 12, 13, and 14 for the drag, lift, and surface vorticity, respectively, all display the same features detailed above for $R = 500$.

To investigate the dependence between the parameters r and β, numerous simulations were carried out whereby the Reynolds number was fixed at $R = 500$ and the inclination was held constant at $\alpha = 45°$. Shown in Figs. 15 and 16 are time variations in the drag and lift coefficients, respectively, over the interval $0 < t \leq 15$ for various values of r and β. Unfortunately, due to numerical instabilities, we were not able to obtain results for $r = 0.2$ with $\beta \neq 0$. From these plots, we are able to make the following observations. First, for a given

Fig. 9 Time variation in C_L for the cases $R = 500$, $r = 0.5$, $\alpha = 45°$, and $\beta = 0, 0.25, 0.5$

Fig. 10 Streamline plots for $R = 500$, $r = 0.5$, and $\alpha = 45°$ at $t = 3, 5, 7, 9, 10, 15$ from top to bottom, respectively, with $\beta = 0.25$ (left) and $\beta = 0.5$ (right)

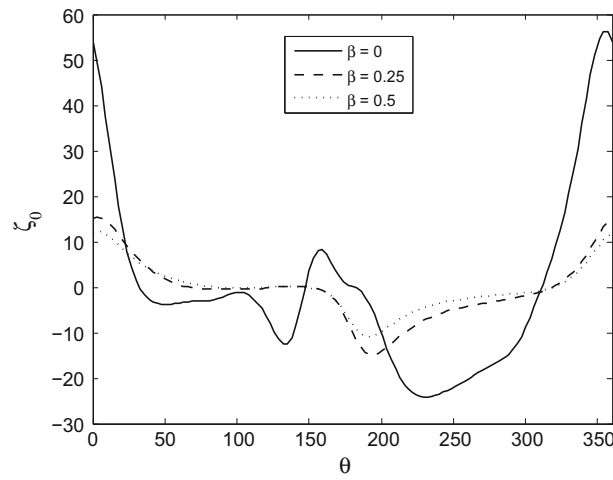**Fig. 11** Surface vorticity distributions at $t = 15$ for $R = 500$, $r = 0.5$, and $\alpha = 45°$ with $\beta = 0, 0.25, 0.5$
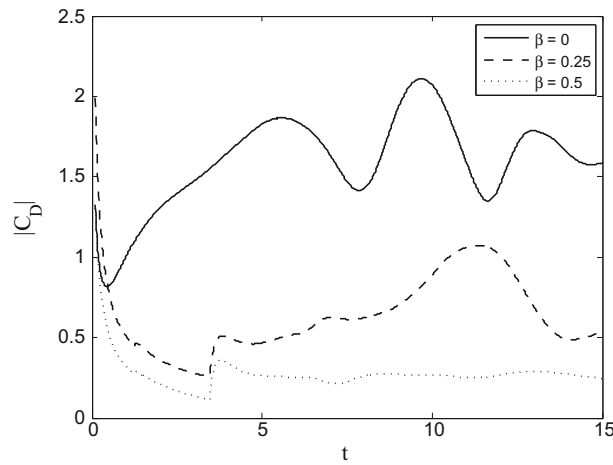

Fig. 12 Time variation in $|C_D|$ for the cases $R = 1000$, $r = 0.5$, $\alpha = 45°$, and $\beta = 0, 0.25, 0.5$
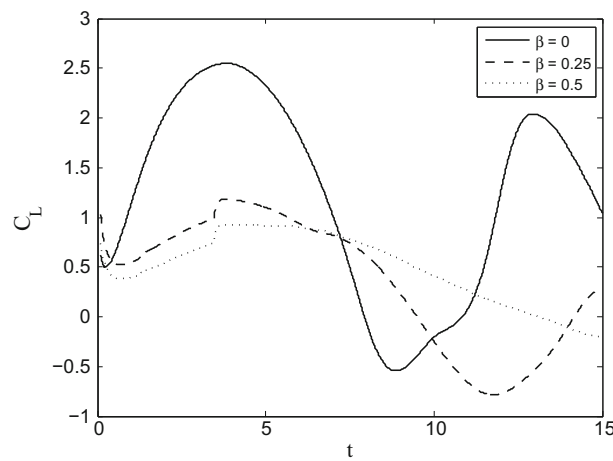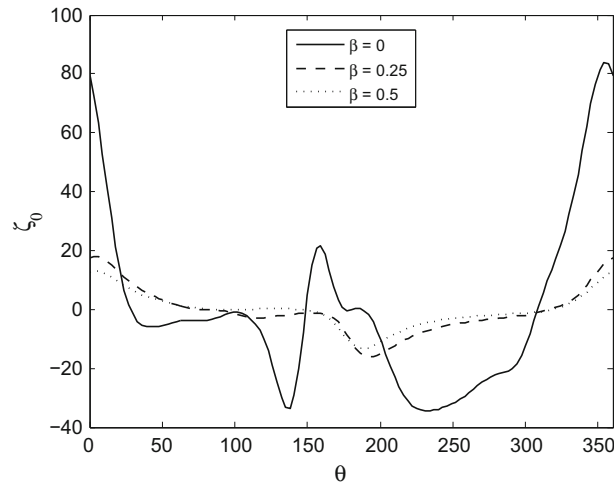

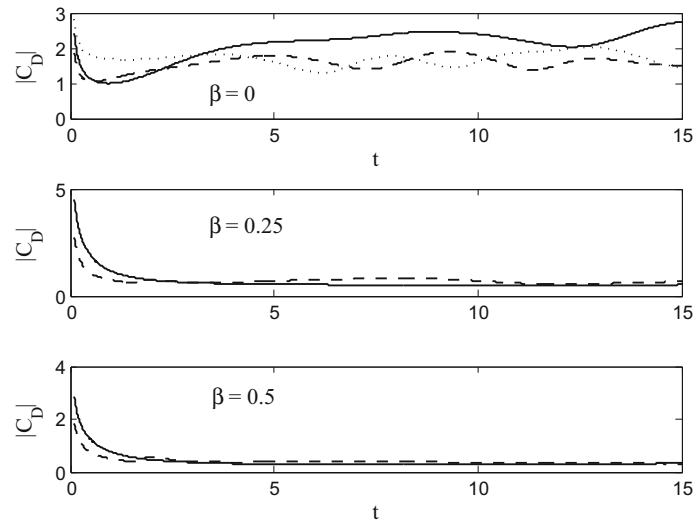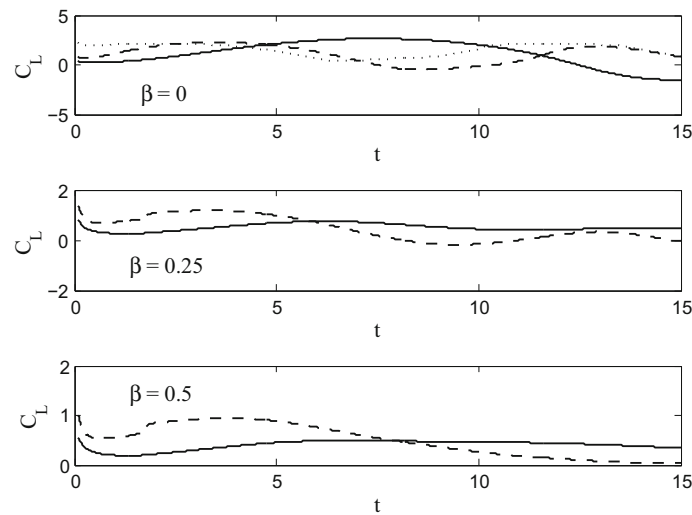**Fig. 13** Time variation in C_L for the cases $R = 1000$, $r = 0.5$, $\alpha = 45°$, and $\beta = 0, 0.25, 0.5$

Fig. 14 Surface vorticity distributions at $t = 15$ for $R = 1000$, $r = 0.5$, and $\alpha = 45°$, with $\beta = 0, 0.25, 0.5$
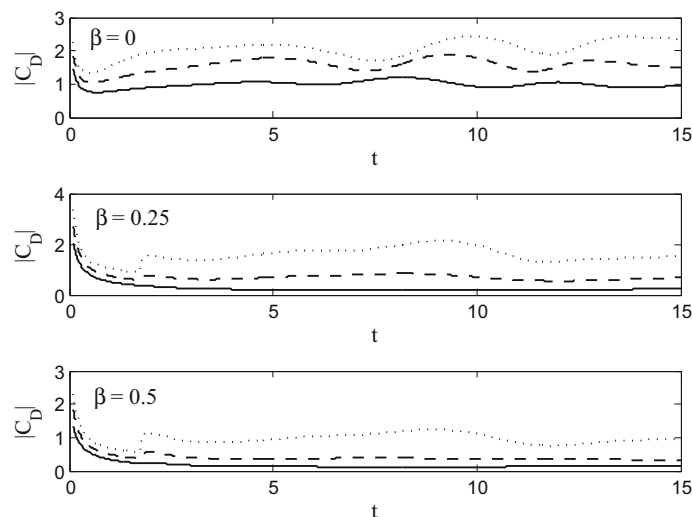

Fig. 15 Time variation in $|C_D|$ for the cases $R = 500$, $\alpha = 45°$, $\beta = 0, 0.25, 0.5$, and $r = 0.8$ (solid line), $r = 0.5$ (dashed line), and $r = 0.2$ (dotted line)

value of β, as r increases, the oscillations in the drag and lift coefficients are reduced. This makes sense since as $r \to 1$ we approach a circular cylinder, and so the flow becomes more symmetric which, as we learned in Part 1, is free of oscillations. Second, as β increases, the drag profiles become flatter and less dependent on the value of r. For example, for $\beta = 0.5$ and $t \gtrsim 2$, the C_D curves for $r = 0.5$ and $r = 0.8$ almost lie on top of each other. Third, as was already noted, the drag decreases as β increases.

Lastly, we explore the relationship between the parameters α and β. To establish this relationship, several numerical experiments were performed whereby the Reynolds number and aspect ratio were fixed at $R = 500$ and $r = 0.5$, respectively. Shown in Figs. 17 and 18 are the results from these simulations. Figure 17 shows the time variations in the drag coefficient while Fig. 18 illustrates the time variations in the lift coefficient. These were done over the time interval $0 < t \leq 15$ for selected values of α and β. From these experiments, we notice that for a specified value of β the drag increases with α as do the oscillations in C_D. This finding comes as no surprise because for small α the flow is more symmetric and streamlined. On the other hand, for a fixed value of α, we see not only a reduction in drag oscillations but also a decrease in the drag as β increases. These observations are consistent with our previous results. As for the lift, for a given value of β, the fluctuations in C_L increase noticeably as the inclination increases. Also, for $\alpha = 30°$ and $\alpha = 45°$, the C_L

Fig. 16 Time variation in C_L for the cases $R = 500$, $\alpha = 45°$, $\beta = 0, 0.25, 0.5$, and $r = 0.8$ (solid line), $r = 0.5$, (dashed line), and $r = 0.2$ (dotted line)
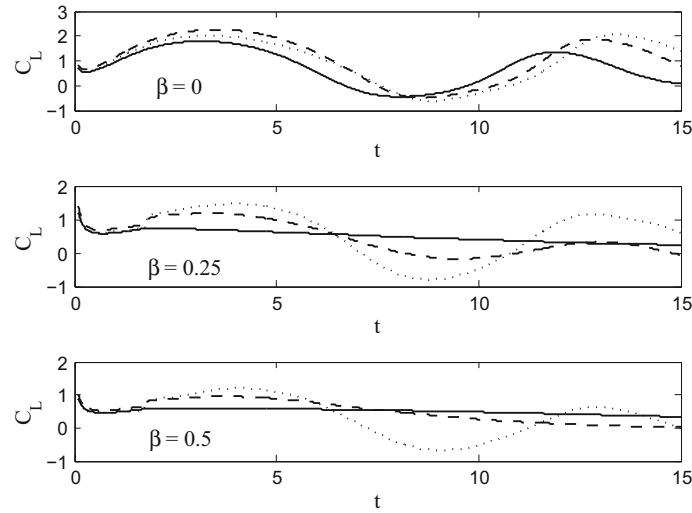

Fig. 17 Time variation in $|C_D|$ for the cases $R = 500$, $r = 0.5$, $\beta = 0, 0.25, 0.5$, and $\alpha = 30°$ (solid line), $\alpha = 45°$ (dashed line), and $\alpha = 60°$ (dotted line)

profiles become flatter as β increases. For $\alpha = 60°$, we see fluctuations in C_L for all values β, although there is a slight reduction as β increases.

5 Conclusions

In Part 2, the unsteady problem of two-dimensional flow of a viscous incompressible fluid past an inclined elliptic cylinder subject to impermeability and Navier slip surface conditions was solved. Two types of solutions have been obtained: an approximate analytical solution in the form of an asymptotic expansion valid for small times and large Reynolds numbers and a numerical solution based on a spectral–finite difference method. These two solutions were found to be in excellent agreement over the appropriate parameter intervals. In addition, comparisons made with previous studies for the no-slip case were also found to be in reasonable agreement.

Numerous numerical experiments were conducted for no-slip and slip cases having Reynolds numbers 500 and 1000. The effect of varying the parameters r, α, and β was also investigated. The asymmetrical case is inherently more complicated and interesting than the symmetric case due to the vortex-shedding process. To our

Fig. 18 Time variation in C_L for the cases $R = 500$, $r = 0.5$, $\beta = 0, 0.25, 0.5$, and $\alpha = 30°$ (solid line), $\alpha = 45°$ (dashed line), and $\alpha = 60°$ (dotted line)

knowledge, no results currently exist in the literature for asymmetrical slip flow past an inclined elliptic cylinder. In addition to the reduction in drag, we have also discovered that vortex shedding undergoes suppression as the slip length increases. Evidence of this comes from the streamline plots as well as the time variations of the drag and lift coefficients. The streamline plots clearly illustrate that the formation of vortices behind the cylinder is delayed as a result of the slip condition. Also, the fluctuations in C_D and C_L associated with vortex shedding can be significantly reduced as β increases. Another feature connected to the slip condition is that, as β increases, there is less variation in the surface vorticity distribution. Lastly, little change in the flow was observed when R was increased from 500 to 1000, that is, all the features observed for $R = 500$ also occurred for $R = 1000$.

Appendix: Derivation of drag, lift, and pressure coefficients

The drag and lift forces acting on a body can be determined by integrating the normal, σ, and shear, τ, stresses around the body surface. The dimensionless stresses in Cartesian coordinates are given by

$$\sigma_x = -P + \frac{4}{R}\frac{\partial U}{\partial x}, \ \sigma_y = -P + \frac{4}{R}\frac{\partial V}{\partial y}, \ \tau_{xy} = \tau_{yx} = \frac{2}{R}\left(\frac{\partial U}{\partial y} + \frac{\partial V}{\partial x}\right). \tag{A1}$$

In the above, (U, V) represent the velocity components in the (x, y) directions, respectively. If l and m denote the direction cosines of the outward normal to the surface where

$$l = \frac{dy}{dS}, \ m = -\frac{dx}{dS}, \tag{A2}$$

with S denoting arc length, then the dimensionless forces on the body per unit length in the x, y directions are

$$X = \oint_C [l\sigma_x + m\tau_{xy} - U(lU + mV)]dS, \ Y = \oint_C [m\sigma_y + l\tau_{xy} - V(lU + mV)]dS, \tag{A3}$$

respectively. Here, C refers to the contour of the body surface. Substituting (A1) and (A2) into (A3) and introducing the vorticity, we arrive at

$$X = -\oint_C P\,dy + \frac{2}{R}\oint_C \zeta\,dx - \oint_C U^2\,dy + \oint_C UV\,dx, \tag{A4}$$

$$Y = \oint_C P \mathrm{d}x + \frac{2}{R} \oint_C \zeta \mathrm{d}y - \oint_C UV \mathrm{d}y + \oint_C V^2 \mathrm{d}x. \tag{A5}$$

We point out that the continuity equation

$$\frac{\partial U}{\partial x} + \frac{\partial V}{\partial y} = 0$$

was also used in obtaining (A4)–(A5). It is also useful to note that the Navier–Stokes equations can be expressed as

$$\frac{\partial U}{\partial t} + \frac{\partial}{\partial x}\left[P + \frac{1}{2}(U^2 + V^2)\right] = -\frac{2}{R}\frac{\partial \zeta}{\partial y} + \zeta\frac{\partial \psi}{\partial x}, \tag{A6}$$

$$\frac{\partial V}{\partial t} + \frac{\partial}{\partial y}\left[P + \frac{1}{2}(U^2 + V^2)\right] = \frac{2}{R}\frac{\partial \zeta}{\partial x} + \zeta\frac{\partial \psi}{\partial y}. \tag{A7}$$

For the elliptic cylinder

$$x = \cosh(\xi + \xi_0)\cos\theta, \quad y = \sinh(\xi + \xi_0)\sin\theta. \tag{A8}$$

Using (A8) it can be shown that for the elliptic cylinder

$$M\frac{\partial v}{\partial t} + \frac{\partial}{\partial \theta}\left[P + \frac{1}{2}(u^2 + v^2)\right] = \frac{2}{R}\frac{\partial \zeta}{\partial \xi} + \zeta\frac{\partial \psi}{\partial \theta} \tag{A9}$$

follows from (A6)–(A7) with the understanding that (u, v) in (A9) represent the velocity components in the (ξ, θ) directions, respectively. After some algebra, it can also be shown that for the elliptic cylinder, (A4)–(A5) become

$$\begin{aligned}
X = {}&\frac{2\sinh\xi_0}{R}\int_0^{2\pi}\left(\frac{\partial\zeta}{\partial\xi}\right)_0 \sin\theta\,\mathrm{d}\theta - \frac{2\cosh\xi_0}{R}\int_0^{2\pi}\zeta_0\sin\theta\,\mathrm{d}\theta \\
&+\frac{\sinh\xi_0}{2}\int_0^{2\pi}(v^2)_0\cos\theta\,\mathrm{d}\theta - \sinh\xi_0\int_0^{2\pi}M_0\left(\frac{\partial v}{\partial t}\right)_0\sin\theta\,\mathrm{d}\theta,
\end{aligned} \tag{A10}$$

$$\begin{aligned}
Y = {}&-\frac{2\cosh\xi_0}{R}\int_0^{2\pi}\left(\frac{\partial\zeta}{\partial\xi}\right)_0 \cos\theta\,\mathrm{d}\theta + \frac{2\sinh\xi_0}{R}\int_0^{2\pi}\zeta_0\cos\theta\,\mathrm{d}\theta \\
&+\frac{\cosh\xi_0}{2}\int_0^{2\pi}(v^2)_0\sin\theta\,\mathrm{d}\theta + \cosh\xi_0\int_0^{2\pi}M_0\left(\frac{\partial v}{\partial t}\right)_0\cos\theta\,\mathrm{d}\theta
\end{aligned} \tag{A11}$$

where we have made use of (A8) and (A9) and

$$(v^2)_0 = \frac{\beta^2 M_0^6 \zeta_0^2}{[M_0^2 + \frac{\beta}{2}\sinh(2\xi_0)]^2}.$$

For the case of no-slip, the last two terms in the expressions for X, Y vanish. Finally, the drag, C_D, and lift, C_L, coefficients in the horizontal and vertical directions, respectively, can then be obtained by a rotation of α given by

$$C_D = X\cos\alpha - Y\sin\alpha, \quad C_L = Y\cos\alpha + X\sin\alpha. \tag{A12}$$

The dimensionless pressure coefficient, defined by $P^*(\xi = 0, \theta, t) = P(0, \theta, t) - P(0, 0, t)$, can be obtained by integrating (A9). Doing this yields

$$P^*(0, \theta, t) = \frac{2}{R}\int_0^\theta\left(\frac{\partial\zeta}{\partial\xi}\right)_0 \mathrm{d}\bar\theta - \frac{1}{2}v^2\big|_0^\theta - \int_0^\theta M_0\left(\frac{\partial v}{\partial t}\right)_0 \mathrm{d}\bar\theta. \tag{A13}$$

For the circular cylinder

$$x = \mathrm{e}^\xi\cos\theta, \quad y = \mathrm{e}^\xi\sin\theta,$$

and for M in (A9), we can substitute e^{ξ}. Using this, it follows that

$$C_{\mathrm{D}} = \frac{2}{R} \int_0^{2\pi} \left(\frac{\partial \zeta}{\partial \xi} - \zeta \right)_0 \sin\theta \, \mathrm{d}\theta + \frac{\beta^2}{2(1+\beta)^2} \int_0^{2\pi} \zeta_0^2 \cos\theta \, \mathrm{d}\theta - \int_0^{2\pi} \left(\frac{\partial v}{\partial t} \right)_0 \sin\theta \, \mathrm{d}\theta,$$

$$C_{\mathrm{L}} = \frac{2}{R} \int_0^{2\pi} \left(\zeta - \frac{\partial \zeta}{\partial \xi} \right)_0 \cos\theta \, \mathrm{d}\theta + \frac{\beta^2}{2(1+\beta)^2} \int_0^{2\pi} \zeta_0^2 \sin\theta \, \mathrm{d}\theta + \int_0^{2\pi} \left(\frac{\partial v}{\partial t} \right)_0 \cos\theta \, \mathrm{d}\theta,$$

$$P^*(0, \theta, t) = \frac{2}{R} \int_0^{\theta} \left(\frac{\partial \zeta}{\partial \xi} \right)_0 \mathrm{d}\bar{\theta} - \frac{\beta^2}{2(1+\beta)^2} \zeta_0^2 \big|_0^{\theta} - \int_0^{\theta} \left(\frac{\partial v}{\partial t} \right)_0 \mathrm{d}\bar{\theta}.$$

References

1. Beavers, G.S., Joseph, D.D.: Boundary conditions at a naturally permeable wall. J. Fluid Mech. **30**, 197–207 (1967)
2. Dennis, S.C.R., Quartapelle, L.: Some uses of Green's theorem in solving the Navier–Stokes equations. Int. J. Numer. Methods Fluids **9**, 871–890 (1989)
3. D'Alessio, S.J.D., Perera, R.N.: Unsteady free convection from elliptic cylinders at large Grashof numbers. Int. J. Heat Mass Transf. **52**, 5940–5953 (2009)
4. Steinmoeller, D.T., D'Alessio, S.J.D., Poulin, F.J.: Prograde and retrograde flow past cylindrical obstacles on a β-plane. Acta Mech. **217**, 157–176 (2011)
5. Dennis, S.C.R., Chang, G.-Z.: Numerical Integration of the Navier–Stokes Equations in Two Dimensions. Mathematics Research Center, University of Wisconsin, Technical Summary Report No. 859 (1969)
6. Staniforth, A.N.: Studies of Symmetrical and Asymmetrical Viscous Flows Past Impulsively Started Cylinders, Ph.D. Thesis, Western University, London, Canada (1972)
7. D'Alessio, S.J.D., Dennis, S.C.R.: A vorticity model for viscous flow past a cylinder. Comp. Fluids **23**, 279–293 (1994)
8. Dennis, S.C.R., Young, P.J.S.: Steady flow past an elliptic cylinder inclined to the stream. J. Eng. Math. **47**, 101–120 (2003)